Turbulent Flow and Endwall Heat Transfer Analysis in a 90° Turning Duct and Comparisons with Measured Data

Part I: Influence of Reynolds Number and Streamline Curvature on Viscous Flow Development

KUISOON KIM*, BRIAN G. WIEDNER[†], and CENGIZ CAMCI[‡]

*Turbomachinery Heat Transfer Laboratory, Department of Aerospace Engineering,
The Pennsylvania State University, University Park, Pennsylvania 16802, USA*

This paper deals with the experimental and computational analysis of flow and heat transfer in a turning duct simulating the overall three-dimensional flow and heat transfer characteristics of gas turbine passages and internal cooling channels. The numerical results obtained for three different Reynolds numbers (790, 40,000, and 342,190) are compared to measured flow characteristics. Extensive measurements of the mean flow structure using a sub-miniature five-hole-probe and a hot-wire provide a quantitative assessment of the computational model used in the analysis. An in-house developed three-dimensional viscous flow solver is the main computational tool of the present study. A well known pressure correction method (SIMPLE) is used for the solution of 3-D incompressible, steady Navier–Stokes equations in a generalized coordinate system. The $k-\epsilon$ turbulence model of Launder and Spalding including a curvature correction scheme is utilized to describe the turbulent flow field. A non-staggered grid system is used in an upwind scheme with additional numerical dissipation terms. It is clearly shown that reducing the artificial dissipation terms in a central differencing scheme reduced the numerical dissipation error. Part II of this paper deals with the convective heat transfer aspects of the specific flow near the endwall surface where three-dimensional viscous flow structures are dominant. The measured fluid mechanics data presented in this paper also provide a reliable data set that can be used in the future validation of new computational methods.

A 90° turning duct is a useful flow configuration to simulate the strong secondary flows existing between the highly cambered blades of axial turbomachinery systems. Turning channels are also frequently used in internal coolant passages of many turbomachinery systems. Turning duct flows are dominated by passage vortices originating from the momentum deficit of the inlet endwall boundary layers. The development of boundary layers on the convex wall and concave wall also affects the turbulent flow structure at the exit plane of a turning duct. The streamlines in the core section of the duct have strong curvature and the three-dimensional mean flow is highly modified by the existence of a pair of counter-rotating vortices and boundary layer flows. In general, secondary flows decay slowly along the streamwise direction of the duct. Convective heat transfer rates on different surfaces of a turning duct differ significantly. Because of the influence of streamline curvature, Thomann (1968) and Mayle et al. (1979) have shown that the heat flux through the concave wall of a curved channel can be up to 33% greater, and through convex wall 15% smaller, than that of the walls of an equivalent straight channel. Complex

*Present address: Dept. of Aerospace Engineering, Pusan National University, Pusan, Korea. E-mail: kuskim@hyowon.pusan.ac.kr
[†]Present address: Brown and Root Energy Services, Texas, USA. E-mail: brian.wiedner@halliburton.com
[‡]Corresponding author. Fax: 814 865 7092. E-mail: C-Camci@psu.edu

three-dimensional flows with secondary flow interacting with the endwalls and the curved surfaces complicate the thermal transport mechanisms in the boundary layers.

Many past experiments have indicated that, in laminar flow, the position of the maximum streamwise velocity moves from the mean radius of the duct towards the pressure surface. In turbulent flow, such migration is initially towards the suction surface and lies at the mean radius at the exit. One of the most detailed measurements about the flow in a curved duct were carried out by Taylor et al. (1981). The measurements of laminar and turbulent flows were performed at Reynolds numbers of 790 and 40,000 in water. The duct was a 90° bend with a mean radius to duct-width ratio of 2.3. Numerical calculations for the laminar and turbulent flows in the same geometry were also performed by Humphrey et al. (1977, 1981). The calculation procedure was based on a numerical method described by Patankar and Spalding (1972). Pratap and Spalding (1975) used similar calculation method to predict a rectangular duct flow at Reynolds number of 7.06×10^5. However, their comparisons with experimental data were only made up to 56° cross-section. Govindan et al. (1991) applied the primary/secondary flow equations in a square cross section duct using a space marching technique including a mixing length model of turbulence.

Recently, Wiedner and Camci (1993) carried out mean flow and high-resolution endwall heat transfer measurements at a Reynolds number of 342,190. This relatively high Reynolds number was chosen because of possible gas turbine implementation. Liquid crystal thermography was used to obtain heat transfer coefficients on the duct surfaces. A comprehensive investigation of streamwise velocity profiles, secondary flow and turbulent flow characteristics as well as heat transfer coefficient distributions at 0°, 45°, and 90° sections were presented.

The primary goal of the present investigation is to assess a widely used finite difference method for the prediction of three-dimensional flow fields in a 90° turning duct. The specific 90° duct geometry and the coordinate system used in this investigation is shown in Figure 1. Many past numerical studies focus on the improvement of numerical accuracy and the influence of curvature effect correction of turbulence model, Leschziner and Rodi (1981). For turbulent flow calculations, contribution to overall error by the specific turbulence model implemented is usually smaller than other errors imposed by the computational building blocks. For example, error contribution due to the numerical dissipation or insufficient grid resolution may be much more significant than the errors introduced by the turbulence model alone. The use of artificial dissipation terms in time marching formulation is well known. However, the practice is not common in SIMPLE method as described by Patankar and Spalding (1972). In the latter, schemes such as the hybrid and power-law might fail to capture the flow field adequately in certain regions. This is especially true in the regions of the flow field where physical diffusion plays no significant role. Consequently, numerical dissipation errors are often observed in those regions. Therefore for the current semi-implicit scheme, second order artificial dissipation terms added to the first order upwind differencing are formulated. The flux terms and convective properties at the control volume faces are
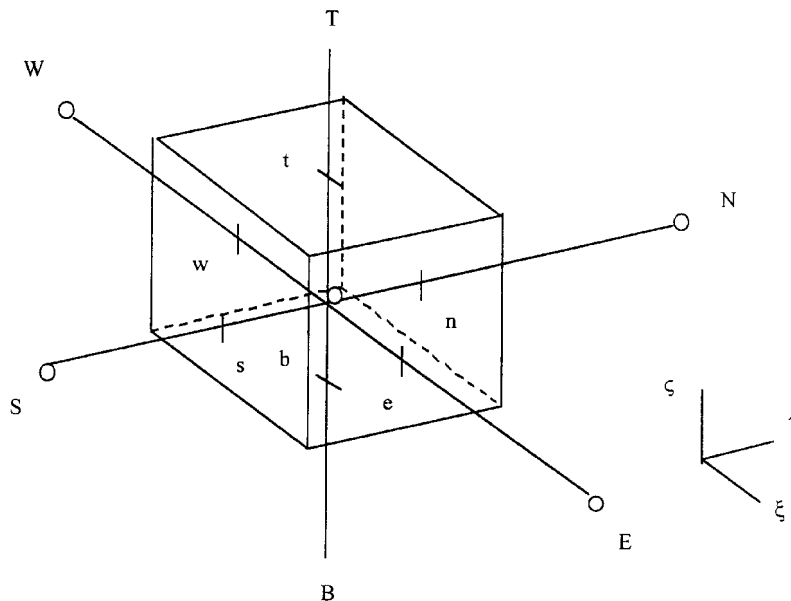

FIGURE 1   90° turning duct geometry and coordinate system.

treated with central differencing. The second order artificial terms are treated explicitly so that a tri-diagonal solver can be formulated in a line relaxation scheme. A detailed discussion on second and fourth order artificial dissipation terms is given by Basson (1992). A non-staggered grid system is used to avoid the extra computational efforts existing in a staggered grid system. To prevent oscillatory pressure solutions due to the use of non-staggered grid, artificial dissipation terms for the pressure correction equation can also be formulated in a similar manner to the momentum equations. Actually, the artificial dissipation terms can be deduced from the pressure-weighting scheme of Rhie and Chow (1983).

THEORETICAL BACKGROUND

For three-dimensional, steady, incompressible, turbulent flow, the set of conservation equations in the Cartesian coordinates are as follows:

$$\frac{\partial}{\partial x}\left(\rho U_x \phi - \Gamma_\phi \frac{\partial \phi}{\partial x}\right) + \frac{\partial}{\partial y}\left(\rho U_y \phi - \Gamma_\phi \frac{\partial \phi}{\partial y}\right)$$
$$+ \frac{\partial}{\partial z}\left(\rho U_z \phi - \Gamma_\phi \frac{\partial \phi}{\partial z}\right) = S_\phi \qquad [1]$$

The corresponding values of the diffusion coefficient Γ_ϕ and the source term S_ϕ for various conservation equations are listed in Table I.

General Transport Equations

The conservation equation for a general dependent variable ϕ can be transformed to an arbitrary curvilinear system (ξ, η, ς). If the grid system is orthogonal, the

TABLE I   Diffusion coefficient and source term for various conservation equations

ϕ	Γ_ϕ	S_ϕ
1	0	0
U_x	$\mu + \mu_t$	$-(\partial p/\partial x)$
U_y	$\mu + \mu_t$	$-(\partial p/\partial y)$
U_z	$\mu + \mu_t$	$-(\partial p/\partial z)$
k	$\mu + \mu_t/\sigma_k$	$G_k - \rho\varepsilon$
ε	$\mu + \mu_t/\sigma_\varepsilon$	$C_1 G_k \varepsilon/k - C_2 \rho \varepsilon^2/k$

resulting transformed equation in the computational plane (ξ, η, ς) is:

$$\frac{\partial}{\partial \xi}\left[\frac{1}{J}\left(\rho G_\xi \phi - g_{11}\Gamma_\phi \frac{\partial \phi}{\partial \xi}\right)\right]$$
$$+ \frac{\partial}{\partial \eta}\left[\frac{1}{J}\left(\rho G_\eta \phi - g_{22}\Gamma_\phi \frac{\partial \phi}{\partial \eta}\right)\right]$$
$$+ \frac{\partial}{\partial \varsigma}\left[\frac{1}{J}\left(\rho G_\varsigma \phi - g_{33}\Gamma_\phi \frac{\partial \phi}{\partial \varsigma}\right)\right] = \frac{S_\phi}{J} \qquad [2]$$

where J is the Jacobian of the transformation.

$$J = \frac{\partial(\xi, \eta, \varsigma)}{\partial(x, y, z)}$$
$$= \frac{1}{x_\xi(y_\eta z_\varsigma - y_\varsigma z_\eta) - x_\eta(y_\xi z_\varsigma - y_\varsigma z_\xi) - x_\varsigma(y_\xi z_\eta - y_\eta z_\xi)} \qquad [3]$$

G_ξ, G_η and G_ς are the contravarient velocity vector components. In the present scheme, all dependent variables in the convection–diffusion equations are defined only at the node P and its neighbors E, W, N, S, T, B as shown in Figure 2. The differential equations of [1] can be expressed
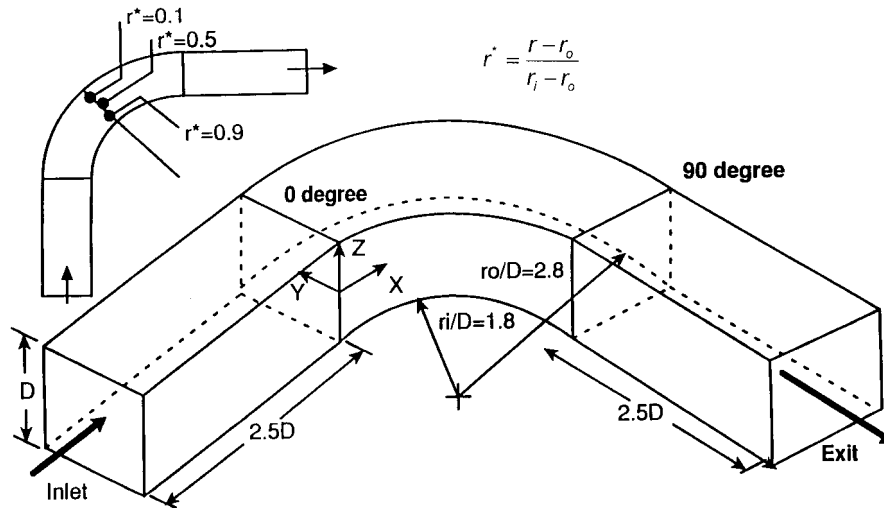

$$r^* = \frac{r - r_o}{r_i - r_o}$$

FIGURE 2   Computational domain definition.

in the following finite-difference form:

$$A_p \phi_p = A_E \phi_E + A_W \phi_W + A_N \phi_N$$
$$+ A_S \phi_S + A_T \phi_T + A_B \phi_B + b \qquad [4]$$

where:

$$A_E = -\frac{1}{2}\left(\rho \frac{G_\xi}{J}\right)_e + \left(\frac{\Gamma}{J}g_{11}\right)_e + \frac{1}{2}\varepsilon_2 \left|\rho \frac{G_\xi}{J}\right|_e$$

$$A_W = \frac{1}{2}\left(\rho \frac{G_\xi}{J}\right)_w + \left(\frac{\Gamma}{J}g_{11}\right)_w + \frac{1}{2}\varepsilon_2 \left|\rho \frac{G_\xi}{J}\right|_w$$

$$A_N = -\frac{1}{2}\left(\rho \frac{G_\eta}{J}\right)_n + \left(\frac{\Gamma}{J}g_{22}\right)_n + \frac{1}{2}\varepsilon_2 \left|\rho \frac{G_\eta}{J}\right|_n$$

$$A_S = \frac{1}{2}\left(\rho \frac{G_\eta}{J}\right)_s + \left(\frac{\Gamma}{J}g_{22}\right)_s + \frac{1}{2}\varepsilon_2 \left|\rho \frac{G_\eta}{J}\right|_s$$

$$A_T = -\frac{1}{2}\left(\rho \frac{G_\varsigma}{J}\right)_t + \left(\frac{\Gamma}{J}g_{33}\right)_t + \frac{1}{2}\varepsilon_2 \left|\rho \frac{G_\varsigma}{J}\right|_t$$

$$A_B = \frac{1}{2}\left(\rho \frac{G_\varsigma}{J}\right)_b + \left(\frac{\Gamma}{J}g_{33}\right)_b + \frac{1}{2}\varepsilon_2 \left|\rho \frac{G_\varsigma}{J}\right|_b$$

$$b = S_U$$
$$A_p = A_E + A_W + A_N + A_S + A_T + A_B - S_P$$

The coefficient ε_2 for the second order artificial dissipation terms can be between zero and one. If ε_2 is equal to one, then the scheme will be reduced to first order upwind scheme. The minimum value of ε_2 may differ for different flow problems because of stability considerations. The quantities S_U and S_P arise from the source term linearization of the form

$$S_\phi = S_U + S_P \phi_P \qquad [5]$$

The Pressure and Velocity Corrections: In order to obtain the velocity field satisfying the continuity equation, a pressure-correction process is employed. The pressure and corresponding velocity corrections are:

$$P = P^* + P' \quad U_x = U_x^* + U_x'$$
$$U_y = U_y^* + U_y' \quad U_z = U_z^* + U_z' \qquad [6]$$

In general, U_x^*, U_y^*, U_z^* will not satisfy the continuity equation. In this approach, the temporary pressure field P^* can be changed such that the resulting starred velocity field will gradually satisfy the continuity equation.

The Pressure Correction Equation

By combining the Eqs. [6] and [2], a pressure correction equation can be obtained. The finite difference form of that still has the same form shown in Eq. [4]. The source term b is the integrated mass flux for the control volume. The coefficients for the pressure correction equation are:

$$A_E = \left(\frac{g_{11}}{J(A_P - \Sigma A_{nb})}\right)_e$$

$$A_W = \left(\frac{g_{11}}{J(A_P - \Sigma A_{nb})}\right)_w$$

$$A_N = \left(\frac{g_{22}}{J(A_P - \Sigma A_{nb})}\right)_n$$

$$A_S = \left(\frac{g_{22}}{J(A_P - \Sigma A_{nb})}\right)_s \qquad [7]$$

$$A_T = \left(\frac{g_{33}}{J(A_P - \Sigma A_{nb})}\right)_t$$

$$A_B = \left(\frac{g_{33}}{J(A_P - \Sigma A_{nb})}\right)_b$$

Turbulent Flow Modeling

Turbulent flow in the present study was simulated using a $k-\varepsilon$ model of Launder and Spalding (1974), in conjunction with the isotropic turbulent viscosity hypothesis. An attempt to investigate the distributions of local turbulent viscosity and streamwise mean velocity was also made with the model of curvature effect correction. The curvature correction method is based on a variable eddy-viscosity coefficient C_μ, modified by the streamline curvature. In general, the amount of turbulent transport in shear layers and size of a re-circulation zone can be influenced by streamline curvature.

The standard turbulence model of Launder and Spalding (1974) contains five empirical constants ($C_1 = 1.45$, $C_2 = 1.90$, $\sigma_k = 1.0$, $\sigma_\varepsilon = 1.3$, $C_\mu = 0.09$). The turbulent eddy viscosity is μ_t, defined as

$$\mu_t = C_\mu \rho \frac{k^2}{\varepsilon} \qquad [8]$$

With the aid of algebraic stress model, the curvature correction to the C_μ coefficient is:

$$C_\mu = \frac{0.09}{1 + 0.57(k^2/\varepsilon^2)((\partial U_s/\partial n) + (U_s/R_c))(U_s/R_c)} \qquad [9]$$

where U_s is the velocity along the streamline, n is the direction normal to it, and R_c is the radius of curvature of the streamline following Leschziner and Rodi (1981). The turbulent production term G_k by definition is as follows:

$$G_k = \mu_t\left[2\left(\frac{\partial U_x}{\partial x}\right)^2 + 2\left(\frac{\partial U_y}{\partial y}\right)^2 + 2\left(\frac{\partial U_z}{\partial z}\right)^2\right]$$
$$+ \mu_t\left[\left(\frac{\partial U_y}{\partial x} + \frac{\partial U_x}{\partial y}\right)^2 + \left(\frac{\partial U_z}{\partial y} + \frac{\partial U_y}{\partial z}\right)^2\right.$$
$$\left. + \left(\frac{\partial U_x}{\partial z} + \frac{\partial U_z}{\partial x}\right)^2\right] \qquad [10]$$

The present study uses the wall function method to eliminate the large number of grid points needed to resolve the laminar sub-layer. It is assumed that the following logarithmic velocity and temperature profiles prevail in the region between the wall and the first grid point,

$$\frac{U_P C_\mu^{1/4} k_P^{1/2}}{(\tau_w/\rho)} = \frac{1}{\kappa} \ln E y_P^+ \qquad [11]$$

$$y_P^+ = \frac{\rho C_\mu^{1/4} k_P^{1/2} y_P}{\mu} \qquad [12]$$

where constants E and κ are respectively 9.739 and 0.4187. The value of $\underline{4}$ for y_P^+ is used to determine the viscous sub-layer thickness. For a simple shear layer, the turbulent kinetic energy k and the dissipation rate ε at the first node from the wall are obtained from the relations of

$$k = \frac{\tau_\omega}{\rho C_\mu^{1/2}} \qquad [13]$$

$$\varepsilon = \frac{k^{3/2}}{y_P C_\mu^{3/4} \kappa} \qquad [14]$$

It should be noted that Eq. [13] is deduced at the local equilibrium condition ($G_k = \rho\varepsilon$). It is not appropriate for separated and stagnation flows.

Boundary Conditions

The geometry under consideration is a square cross section, 90° turning duct as shown in Figure 1. The mean radius to the duct–width ratio is 2.3. Only one-half of the turning duct is computed because of the symmetry, the grid has $81 \times 49 \times 33$ grid points in the streamwise, radial, spanwise directions. The computations were performed on CRAY YMP facilities at NASA Lewis Research Center. The flow solutions were considered to be numerically converged when sum of mass flux residuals at all nodes was less than 0.1% of the inlet mass flux. The convergence of the mean flow solution required approximately 1 hour of CPU time.

On the wall boundaries, no-slip conditions and normal pressure gradient equal to zero were applied. At the symmetry plane $Z = 0$, $(\partial(\ )/\partial Z) = 0$ was required for all the dependent variables. The inflow conditions for laminar (Re = 790) and turbulent flow (Re = 40,000, 342,190) were prescribed from the measured data at $X = -0.5D$, $-0.25D$ and $-2.75D$ respectively. In the absence of experimental data in the Z direction, U_Z was set to zero. This was a good approximation since the cross-flow in the bend was initially weak. The inlet turbulent kinetic energy level was computed from the measured values of the streamwise velocity

fluctuations based on the isotropic turbulence assumption.

$$k_{\mathrm{in}} = \frac{3}{2} u_{\mathrm{in}}^2 \qquad [15]$$

The profile of inlet dissipation rate $\varepsilon_{\mathrm{in}}$ was found from:

$$\varepsilon_{\mathrm{in}} = \frac{k_{\mathrm{in}}^{3/2}}{0.01D} \qquad [16]$$

At the exit of the duct, the fully developed flow conditions were specified, i.e., $(\partial(\ )/\partial\varsigma) = 0$.

EXPERIMENTAL/NUMERICAL RESULTS AND DISCUSSION

The numerical predictions of three-dimensional flow in the 90° turning duct and comparisons to measured aerodynamic data are discussed in this section. The computational and experimental results for flows at Reynolds numbers of 790 (laminar, low Re), 40,000 (turbulent, intermediate Re) and 342,190 (turbulent, high Re) are presented. The experimental water flow data of Taylor et al. (1981) in a duct of $40 \times 40 \, \mathrm{mm}^2$ cross section are used for the comparison of laminar and intermediate Reynolds number cases. The mean radius to the duct width ratio is 2.3 and the bulk inlet velocities are 1.98 cm/s and 1.002 m/s for the laminar and turbulent flows, respectively. For lack of measured water flow data at geometric inlet of the duct, the numerical computations are started at $0.5D$ and $0.25D$ ahead of the bend for the laminar and turbulent flows (intermediate Re), respectively. The upstream effects of the bend are incorporated through initial conditions derived from experimental data at the starting planes.

Another extensive experimental investigation of air flow in a square turning duct (also of mean radius to width ratio of 2.3) by Wiedner and Camci (1993) is used to validate the numerical solution at high Reynolds number, Re = 342, 190. The Reynolds number is based on the bulk inlet velocity of 26.9 m/s and the duct width of 0.203 m. The inlet turbulent kinetic energy is obtained from the measured streamwise turbulent velocity fluctuations, using Eq. [15]. Experimental results from the inlet section confirm the existence of a reasonably isotropic turbulent flow field. The computation is started at $2.75D$ ahead of the bend with available measured data as initial conditions. The coordinates used in the figures follow the convention used by Taylor et al. (1981). The radial coordinate r^* varies from 0 at the concave wall to 1 at the convex wall. The spanwise coordinate Z/D varies from 0 at the symmetry plane to 0.5 at the top endwall. The streamwise coordinate X is perpendicular to the radial direction. The minus sign for X represents the upstream region of 0° cross section,

while the positive X represents the downstream region. Another coordinate $Y = (1 - r^*)$ was also used in order to be consistent with the convention used by Wiedner and Camci (1993).

Low/Intermediate Reynolds Number
Water Flow

The laminar water flow case (Re = 790) which may avoid some of the additional uncertainties introduced by turbulence modeling was used to study the numerical performance of the computational method. A laminar water flow case is also an ideal environment to investigate the influence of numerical dissipation on the numerical results. Figures 3a and 3b show the streamwise mean velocity distributions

at $X = 77.5°$ and $X = 0.25D$ sections, respectively. For this low Reynolds number flow case, viscous effects dominate the entire flow region. The numerical dissipation generated by the viscous term in momentum equation becomes a significant error source in the calculation. When ε_2 equals to 1, the current scheme is identical to the first order upwind formulation and fails to capture the strength and location of the secondary flow vortex accurately. The discrepancy between the calculated results and experimental data is visible due to the numerical dissipation. The strong velocity gradients associated with the secondary flow are most obvious near the convex wall ($r^* = 0.5$, 0.7 and 0.9). Among these, a maximum error upto 23% exists at $r^* = 0.9$ of 77.5° section. At $X = 0.25D$, this dissipation phenomena turns out to be more pronounced near the convex wall and a
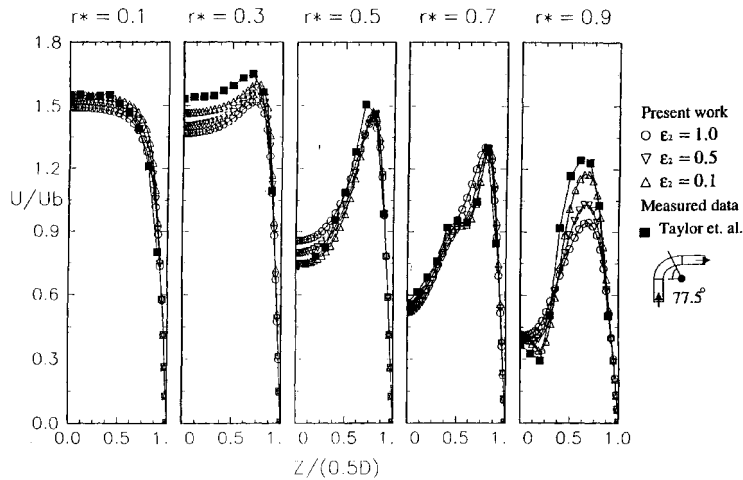

FIGURE 3a   Influence of artificial dissipation coefficient ε_2 on streamwise mean velocity, $X = 77.5°$ and comparison with experimental data (Re = 790, water flow).
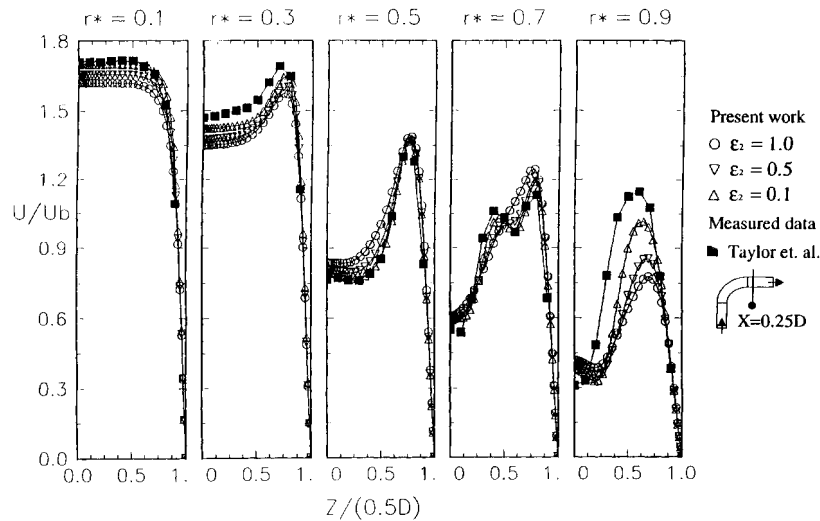

FIGURE 3b   Influence of artificial dissipation coefficient ε_2 on streamwise mean velocity, $X = 0.25D$ and comparison with experimental data (Re = 790, water flow).

maximum error of 32% was found at $r^* = 0.9$. As ε_2 is decreased, further reduction in artificial dissipation significantly improves the solutions. However, due to the instability of central differencing scheme, ε_2 can never go down to zero. The lower limit of ε_2 was found to be 0.1 for this particular case. For the case of higher Reynolds number flow, the weaker influence of the physical diffusion leads to the higher values for the lower limit of ε_2. For Re = (40,000 and 342,190), the lower limits of ε_2 are (0.6 and 0.8) respectively, as shown in Figures 4 and 5.

The standard $k - \varepsilon$ model (Launder and Spalding, 1974) was utilized to describe the turbulent flow field. Although this model is originally developed for flows with low Reynolds number, it is applicable to the complete duct flow. Even though the core flow may have a high Reynolds

number character, the flow near the walls are considered to be low Reynolds number because convection effects are not large compared to diffusion effects. Therefore, for the current high Reynolds number flow case, the overall simulation was still based on this model. For turbulent flow at Re = 40,000, the computation was started at $0.25D$ ahead of the curved duct in a similar manner to the laminar flow calculation. The available experimental data only provided velocity and turbulent fluctuation profiles at $r^* = 0.1$ and $r^* = 0.9$ for the near-wall region. There was no information about initial boundary layer profiles inside the near-wall regions where r^* is less than 0.1 and greater than 0.9. Streamwise mean velocities for turbulent flow (Re = 40,000) at 77.5° and $X = 0.25D$ sections were plotted in Figures 4a and 4b. The line distributions of streamwise
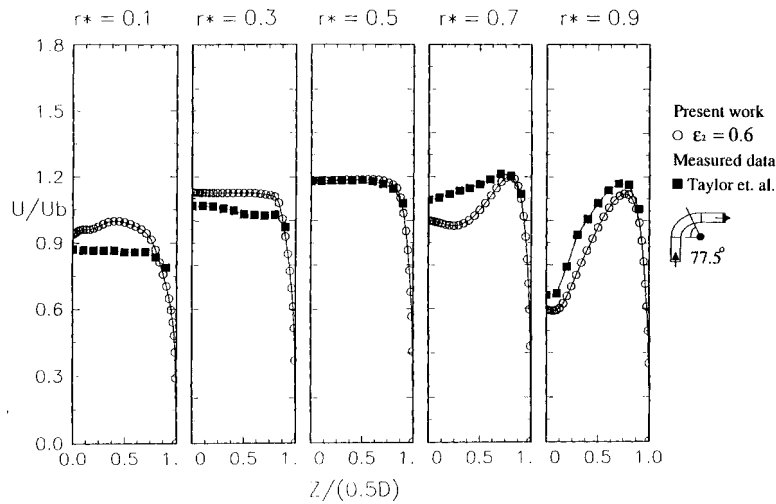

FIGURE 4a   Prediction for intermediate Re, water flow at $X = 77.5°$ and comparison with measured data (Re = 40,000).
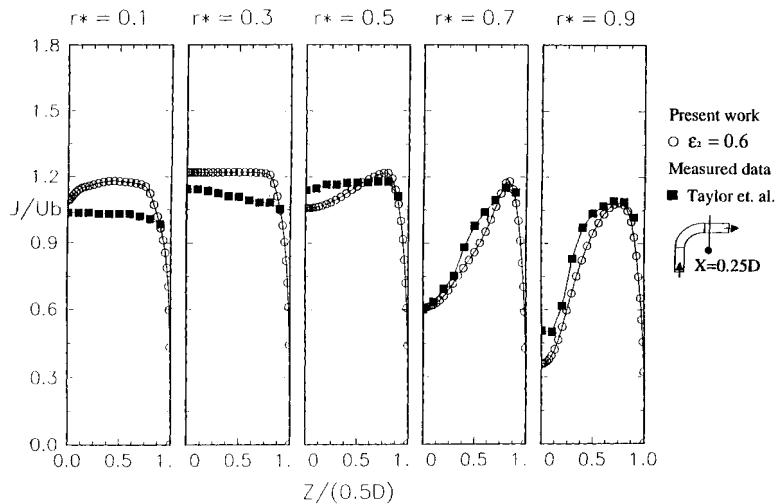

FIGURE 4b   Prediction for intermediate Re, water flow at $X = 0.25D$ and comparison with measured data (Re = 40,000).

velocity are along the height of the duct (Z/D) for a specified radial position $r^* = ((r_o - r)/(r_o - r_i))$. The current numerical scheme gave rather good predictions for the strength of the secondary flow vortex. The observed error near the concave wall ($r^* = 0.1$ and $r^* = 0.3$) might be caused partly by the lack of initial boundary layer profiles in the water flow data of Taylor et al. (1981). The existence of a strong streamline curvature near the concave wall may also contribute to the observed error for small values of r^*. The concave wall with destabilizing curvature had high
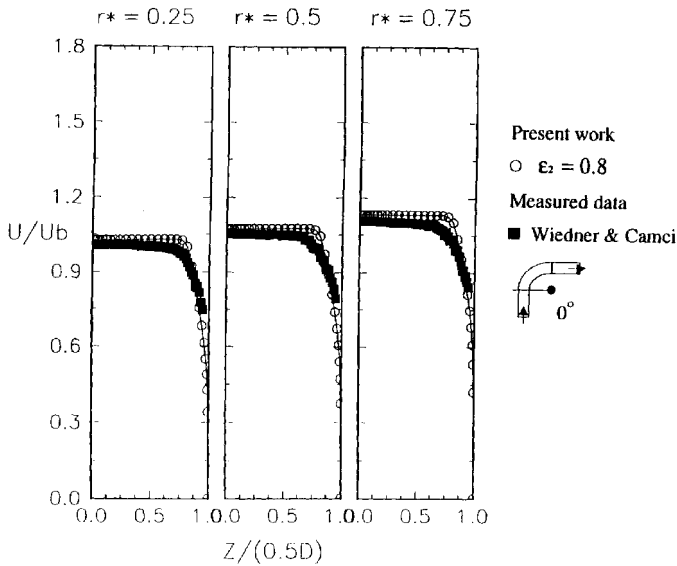

FIGURE 5a   Prediction for Re = 342,190 at $\underline{X} = \underline{0}°$ and comparison with measured data.
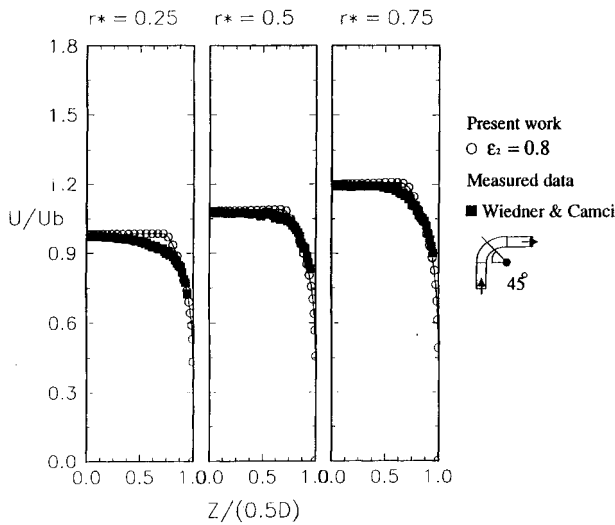
FIGURE 5b   Prediction for Re = 342,190 at $\underline{X} = \underline{45}°$ and comparison with measured data.
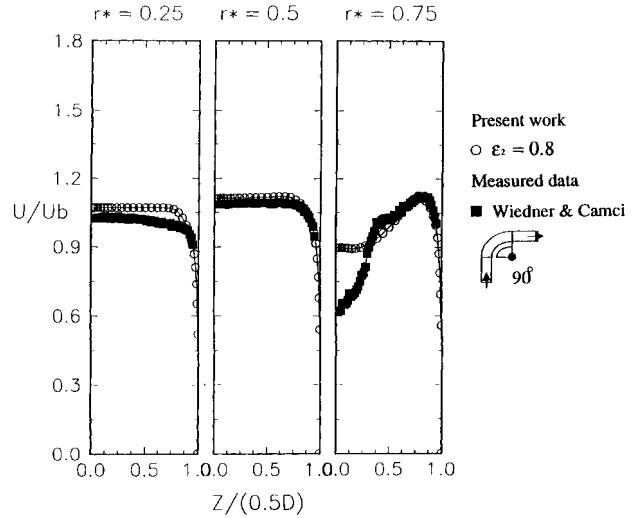
FIGURE 5c   Prediction for Re = 342,190 at $\underline{X} = \underline{90}°$ and comparison with measured data.

levels of Reynolds stress and turbulent kinetic energy, while the convex wall with stabilizing curvature had lower turbulent kinetic energy. In general, the passage vortex system induces cross-flows on the flat endwall surfaces in a direction from the concave wall to convex wall. This cross-flow effect becomes stronger as one approaches the exit section of the duct, Wiedner (1994). It is likely that high turbulence fluid near the concave surface can be convected to the convex side of the duct near the endwall surfaces.

In these two cases, both flows approaching the bend were fully developed. In the laminar flow case, the maximum streamwise velocity position moved rapidly towards the concave wall from the beginning of the bend and tended to stay there. In the turbulent flow case with intermediate Reynolds number, the locus of the maximum streamwise velocity moved towards the convex wall and then turned to the center of the bend before exit. The secondary flows in the laminar flow (Re = 790) were more pronounced than in the turbulent flow (Re = 40,000) because of the thicker boundary layer at the inlet of the bend.

High Reynolds Number Air Flow

The endwall boundary layer details for high Reynolds number turbulent flow (Re = 342,190) at 0°, 45°, and 90° cross-sections were presented in Figure 5. The numerical results showed very good agreement with the experimental data except near the symmetry plane ($r^* = 0.75$) of 90° cross-section as shown in Figure 5c. At this location, a strong velocity gradient associated with the passage vortex occurred and a 38% over-prediction was observed in the numerical solution. In this region, the isotropic turbulence assumption and "wall function," which models the near

wall layer based on simple flow experiments may not hold. $r^* = 0.75$ location is near the convex side of the duct where the two counter rotating passage vortices interact. The core region of the streamwise mean velocity was over-predicted and behaved like an inviscid flow with higher momentum near the convex wall and lower near the concave wall, from $X = 0°$ to $X = 45°$. The maximum velocity point moved from the inner wall to the center of the duct, as observed in the previous turbulent water flow case (Re = 40,000).

Another observation at Re = 342,190 was made on the development of streamwise mean velocities at mid-span of $0°$, $45°$, and $90°$ cross sections as shown in Figure 6. At $0°$ section the influence of the bend on the upstream flow was evident with higher velocity near the inner wall. Then the fluid particles continued to accelerate up to $X = 45°$ along the inner wall. At the $90°$ plane, the core of high momentum fluid moved to the mean radius and a slight velocity defect was observed near the suction side. The velocity defect near the convex surface corresponds to passage vortex

FIGURE 6 Streamwise mean velocity at mid-span (Re = 342,190) Horizontal plane ($Y/D = 0$ convex wall, $Y/D = 1$ concave wall).

interaction area at the mid-span location. Between $Y/D = 0.1$ and 0.375, the numerical scheme showed a deviation from the experimental results, as previously observed in the plot of the endwall boundary layer profile in Figure 5c. It should be noted that in this area, a pair of counter rotating passage vortices interacted with each other such that a highly three-dimensional flow zone was formed. An experimental confirmation of this interaction is fully described in Wiedner (1994). Therefore, the current turbulence model with the assumptions of isotropic turbulent property and scalar empirical constants was not capable of capturing the turbulent structure in this region.

Mean Vorticity Components

The distribution of streamwise mean vorticity Ω_x across the passage at $90°$ section is shown in Figure 7a. The negative contour values appear near the convex surface of the duct. Near the wall, high velocity gradients result in strong vorticity zones. The experimental measurement can not usually resolve the "near wall" regions in extreme detail. In addition to the two primary passage vortices, a second measured vortex pair is found near the inner radius surface, which had negative sign. The generation of the "*second vortex pair*" was the intense interaction of the two passage vortices and the convex inner wall surface. These two pairs resulted in a highly unsteady three-dimensional flow structure and played an important role in the local level of total pressure at the passage exit. Some of the measured five-hole-probe data presented in Wiedner (1994) also confirm the "*second vortex pair*."

The transverse components of vorticity can be estimated from Helmholtz equation that is derived for a steady, rotational, inviscid and incompressible flow field in the absence of body forces. The radial and vertical components of vorticity in Helmholtz equation are respectively:

$$\Omega_Y = \frac{1}{U}\left(+\frac{1}{\rho}\left(\frac{\partial P_o}{\partial Z}\right) + V\Omega_X\right)$$

$$\Omega_Z = \frac{1}{U}\left(-\frac{1}{\rho}\left(\frac{\partial P_o}{\partial Y}\right) + W\Omega_X\right)$$

[17]

Therefore, with measured U, V, W components and the gradients of the stagnation pressure in a single measurement plane of interest, the transverse components of vorticity (Ω_Y and Ω_Z) can be estimated. In the computational approach, all three components of vorticity are directly available. They are from a "viscous" flow solution instead of an "inviscid" approach as approximately predicted by Helmholtz equation. For the highest Reynolds number case (Re = 342,190), most of the core flow region can be assumed to be inviscid so that it is interesting to
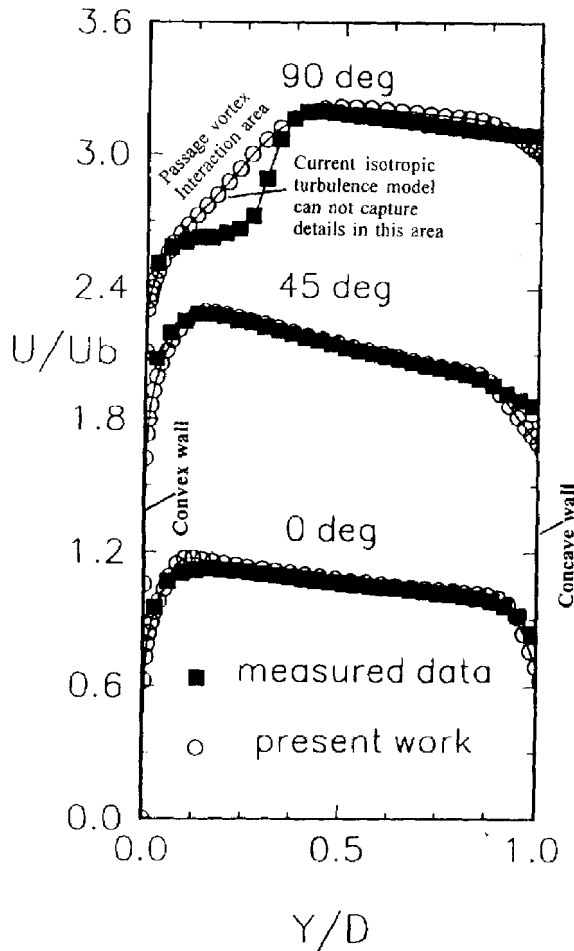
make a comparison with the numerical solution through the Helmholtz equation. Figures 7b and 7c show the radial (Ω_Y) and vertical mean vorticity (Ω_Z) at 90° cross section. In general, the numerical results (from a viscous solution) were quantitatively in good agreement with the measured data (only Ω_X measured, Ω_Y and Ω_Z re-constructed from the inviscid Helmholtz equation). In Figure 7c, the general contour shape near the inner wall was captured for the spanwise mean vorticity (Ω_Z), but the positive zone near the concave wall was not present in the experimental result.
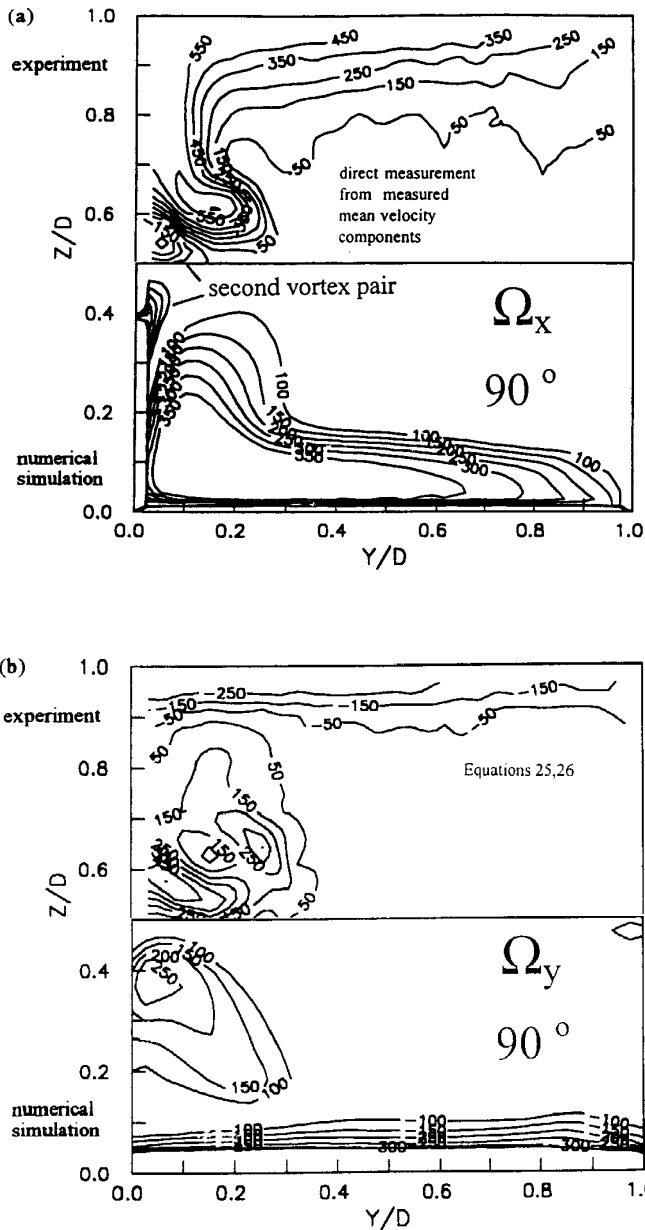

FIGURE 7 (Continued).

Measured and Computed Total Pressure at 90° Cross Section

Figure 8 presents a comparison of measured and computed total pressure losses at 90° cross section of the duct. High aerodynamic loss regions are located near the convex surface of the duct between the inner surface and the two counter-rotating passage vortices. The losses in mean kinetic energy of the flow are significant in this region

FIGURE 7 Comparison of measured and numerically predicted mean vorticity [1/sec] (Re = 342,190) (a) streamwise Ω_x, (b) radial Ω_y, (c) spanwise Ω_z.
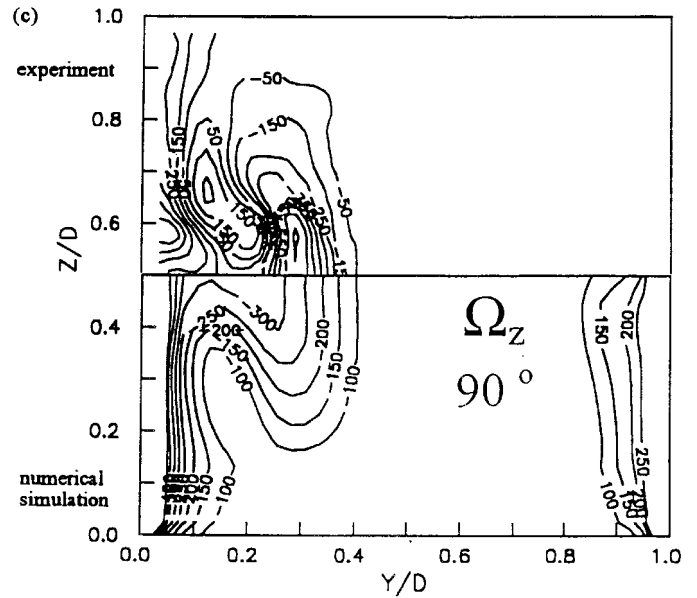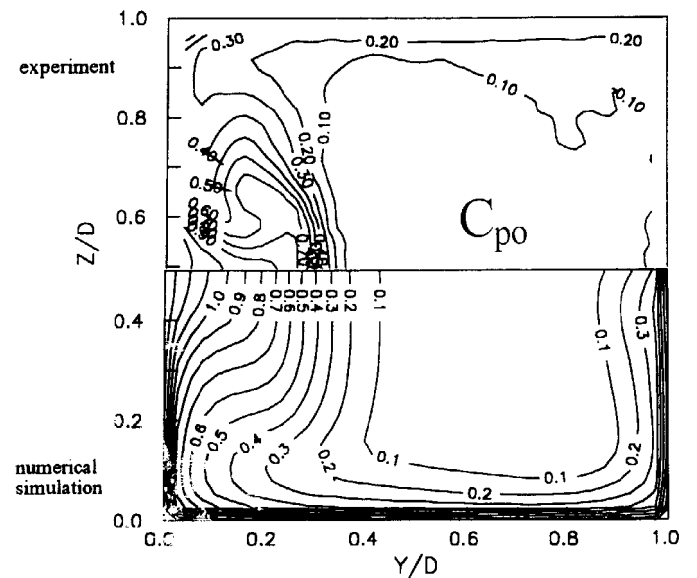

FIGURE 8 Comparison of measured and numerically predicted total pressure coefficient C_{po} at 90° cross section (Re = 342,190).

where the two counter rotating passage vortices interact with the convex surface.

The predictability of the measurements near the convex wall is reduced as one moves toward the interaction area near the mid-span, $(Z/D=0)$. Extremely high strain rates in this highly rotational fluid flow region increases the viscous losses and reduces the predictability of the viscous flow in this area. The overall "mushroom shape" of the passage-vortex/convex-wall interaction area is apparent in both measurements and computations, Figure 8. More details about the aerodynamic features of this area can be found in Wiedner and Camci (1997). The same reference also contains detailed information about the details of the associated measurement uncertainties.

Influence of Streamline Curvature and Effective Viscosity

The influence of streamline curvature in turbulent flow predictions can be taken into account by using a model suggested by Leschziner and Rodi (1981). Figure 9 presents the influence of local streamline curvature on the amount of local turbulent viscosity considered in the present two-equation model calculations. In a two-equation model, turbulent viscosity is calculated from the local dissipation rate and turbulent kinetic energy via $\mu_t = C_\mu \rho k^2/\varepsilon$. This model accounts for the influence of streamline curvature on μ_t by modeling the C_μ coefficient using Eq. [9]. The effective viscosity $\mu_{\text{eff}} = \mu_{\text{lam}} + \mu_t$ is plotted in Figure 9 in function of Y/D for Re $=40,000$ and $342,190$. The results are presented in the horizontal plane $(Z/D=0)$ from the convex surface $(Y/D=0)$ to concave surface $(Y/D=1)$. In either case of the intermediate and high Reynolds number turbulent flows, significant additions to laminar viscosity are observed near the inner wall of 90° section, where intense interactions of passage vortices existed. It should be noted that the high Reynolds number flow (Re $=342,190$) appeared to have reduced turbulent viscosity near the concave wall when curvature correction is applied, as shown in Figure 9a. Curvature correction slightly reduces the effective viscosity μ_{eff} near the concave wall for both Reynolds numbers. Modification for Re $=40,000$ near the concave wall is minimal (reduction in μ_{eff}) as shown in Figure 9b.

Figure 9 clearly shows that a significant portion of the duct cross section is dominated by laminar flow where μ_t is nearly zero. For 0° and 45° cross sections, the area between the convex wall boundary layer edge and the concave wall boundary layer edge is free from turbulent action. At high Reynolds number, the laminar zone is predicted between $Y/D=0.1$ and $Y/D=0.8$ in the horizontal plane passing from $Z/D=0$. At 45° cross section a slightly larger area near the convex side is dominated by turbulent flow.
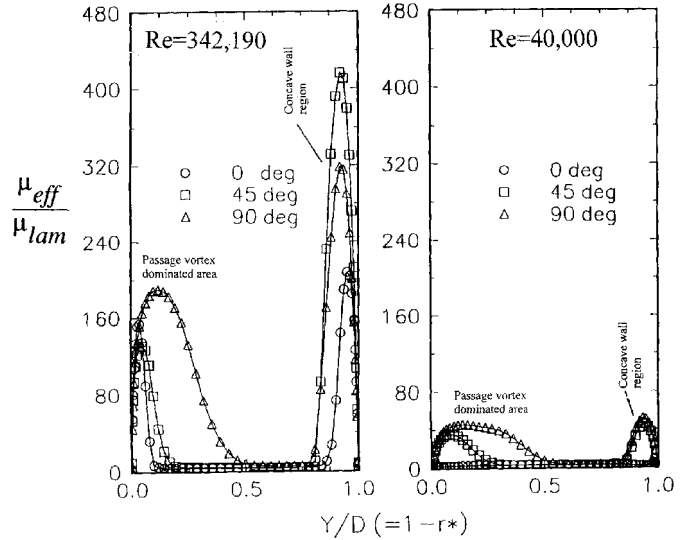

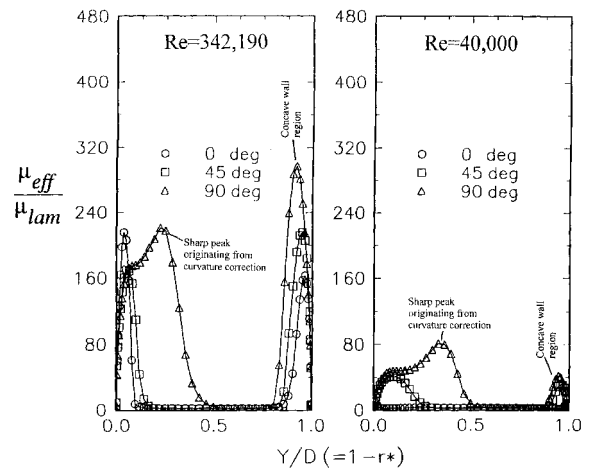FIGURE 9a   Turbulent viscosity *without* curvature correction.

FIGURE 9b   Turbulent viscosity *with* curvature correction.

Significant turbulent activity is confined into wall shear layers where convex and concave curvature is dominant. At intermediate Reynolds number, turbulent flow area coverage near the concave wall is slightly reduced when compared to high Reynolds number case. Although the curvature correction near the concave surface has a tendency to modify effective viscosity magnitude in this area, it does not influence the area coverage of turbulent flow in a significant manner.

Figures 9a and 9b suggest that the area covered by turbulent flow is significantly expanded by the existence of passage vortices. Figure 10 shows that the convex wall region with turbulent flow character is extended up to $Y/D=0.5$ at the exit cross section. At 90° cross section, the influence of highly rotational passage vortex on turbulence production is clear in $\mu_{\text{eff}}/\mu_{\text{lam}}$ distributions along Y/D
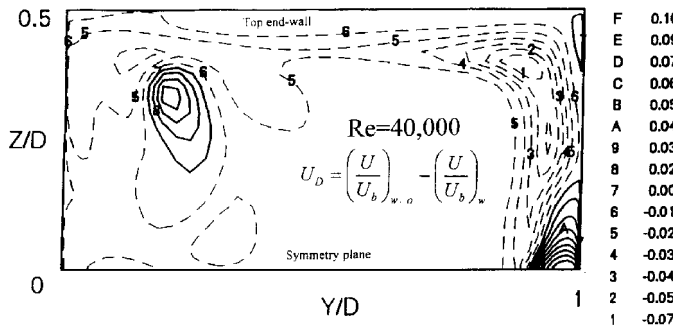
FIGURE 10a Mean velocity difference U_d at 90° cross section (Re = 40,000).

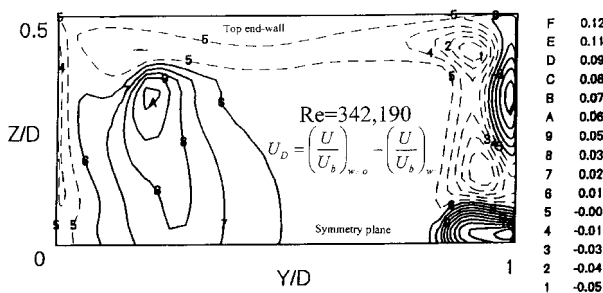
FIGURE 10b Mean velocity difference U_d at 90° cross section (Re = 342,190).

(at $Z/D = 0$). At 45° cross section, turbulent flow dominated area is almost four times less than the coverage in 90° section. At 0° and 45° cross sections, the major contributor to turbulence production is the convex wall boundary layer ($Y/D \leq 0.15$). At 45°, the initial growth of the passage vortex produces a slight increase in turbulent flow area coverage compared to 0° cross section. The observed turbulent flow area coverage from computations are similar for both high and intermediate Reynolds number cases. However, for Re = 40,000, the average magnitude of effective viscosity μ_{eff} is 3 to 6 times smaller in turbulent flow areas when compared to high Reynolds number case. Figure 9 shows that a smoothly varying effective viscosity curve between the convex wall and concave wall ($Y/D < 0.5$) can be easily modified by the curvature modification imposed by the passage vortex pair in the passage. The sharp peak appearing around $Y/D = 0.2$ in Figure 9b is a good example of the curvature modification suggested by the passage vortex system (Re = 342,190). The curvature correction produced peak in effective viscosity is also apparent with a small shift to higher Y/D in intermediate Reynolds number curve ($Y/D = 0.3$). At intermediate Reynolds number, the passage vortex covers a larger area when compared to its high Reynolds number counterpart. A good experimental visualization of the passage vortices described in this paper are presented in

Wiedner and Camci (1996). The measurements of the three components of the mean velocity vector confirm that the core of the passage vortex and the peak observed around $Y/D = 0.2$ in Figure 9b coincide.

Although the immediate result of curvature correction is on the predicted effective turbulent viscosity level, calculated mean velocities are significantly affected from the corrections already described. Alterations in the velocity field result in because of the modified turbulent force term in the momentum equation. While the area coverage of turbulent flow is modified, the changes in the magnitude of effective viscosity also result in significant alterations in the mean velocity field. Figure 10 shows the change in the streamwise mean velocity due to curvature correction for intermediate and high Reynolds number cases. The percentage velocity change U_D is defined as $U_D = (U/U_b)_{w/o} - (U/U_b)_w$ where the subscript "w/o" denotes the model without curvature effect correction and "w" denotes the one with curvature effect correction.

Comparisons between the standard $k - \varepsilon$ model of Launder and Spalding (1974) and modified turbulence model with curvature effect correction of Leschziner and Rodi (1981) are illustrated in Figure 10. In general the modified turbulence model predicted the normalized streamwise velocities upto $10 - 12\%$ (of U_b) lower than the standard model near the mid-span ($Z/D = 0$) of the concave surface for both Re = 40,000 and 342,190. Similar trends as indicated by solid lines exist near $Z/D = 0.3$ in the concave wall boundary layer. The modifications due to curvature correction occur in various zones in the duct cross section. The important modification areas are concave wall boundary layer, top (or bottom) end-wall boundary layers, core of the passage vortex near the convex wall and the interaction zone between the passage vortex and the convex wall. Solid lines in Figure 10 indicate the reduced streamwise velocity resulting from the modified turbulence model. Dashed lines indicate slight increases in velocity resulting from of curvature correction.

A 4% to 6% under-prediction of streamwise velocity in the core of the passage vortex ($Y/D < 0.5$ and $Z/D < 0.4$) is apparent in Figure 10. The area between the dashed contour line 4 ($U_d = -0.01$) and solid line 6 ($U_d = +0.01$) in Figure 10b is the core flow zone in which the curvature correction has almost no influence on velocity predictions. This area coincides with the core flow zone (Re = 342,190) in which viscosity does not have a strong contribution. Details of the measured aerodynamic field in this section can be found in Wiedner and Camci (1997).

Measured and Computed Turbulent Kinetic Energy

Figure 11 shows a comparison of estimated turbulent kinetic energy from the computations and measured
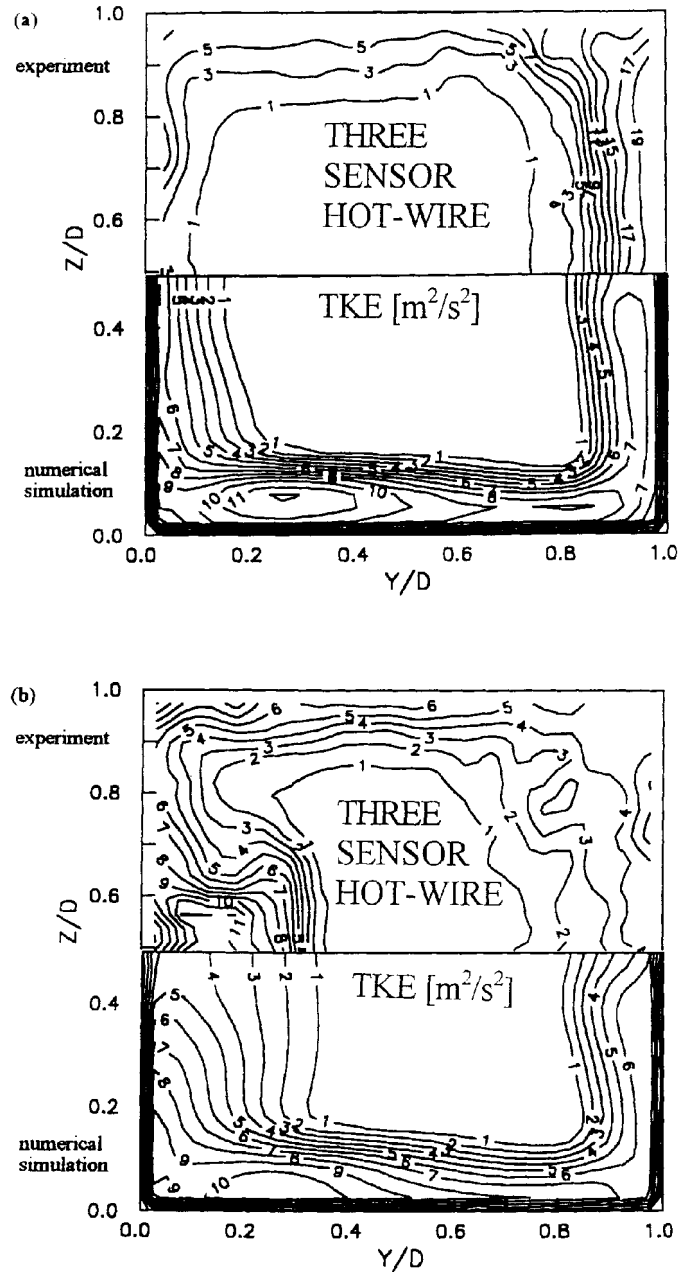
FIGURE 11 Comparison of experimentally measured and numerically determined turbulent kinetic energy TKE Re = 342,190 (a) 45° cross section (b) 90° cross section.

turbulent kinetic energy *via* three sensor hot-wire measurements performed at Re = 342,190 by Wiedner and Camci (1996). The accuracy for a typical turbulent kinetic energy measurement is about ± 0.74 (m²/s²) evaluated at 5.0 (m²/s²). Figure 11 indicates that the order of magnitude variation of turbulent kinetic energy is reasonably simulated by the current model. Similar levels of turbulent activity is observed in the endwall boundary layer (near $Z/D = 1$, $0 < Y/D < 1$) both in computations and measurements. Measured and computed turbulent kinetic energy

magnitudes in the concave-wall boundary layer are also similar. Although one should not expect to predict turbulent kinetic energy in this complex flow from a two-equation model originally developed from parallel flow ideas, it is obvious that qualitative trends can be simulated. At 45° and 90° cross sections, endwall boundary layer and concave wall boundary layer simulations are reasonably comparable to measurements. Figure 11b clearly indicates that the extremely complex passage vortex interaction area in the 90° cross section can not be described accurately by

the computations. Although the overall magnitudes are close, the mushroom shaped passage vortex interaction area that is clearly visible in the hot-wire measurements can not be captured by the current two-equation model including the curvature correction. Three-dimensional re-circulatory flows are so dominant near the core of the passage vortices and in the interaction zone between the passage vortices, a two-equation model originally developed from a pure shear flow idea is not sufficient. Three-sensor hot-wire measurements performed by Wiedner and Camci (1996) clearly show that the passage vortex interaction area at the 90° cross section coincides with turbulent stress measurements confirming the an-isotropy of the field.

CONCLUDING REMARKS

The current study presents detailed fluid mechanics information simultaneously for a fully laminar and mostly turbulent three-dimensional turning duct flow.

The laminar water flow case at $Re = 790$ is effective in studying the influence of numerical dissipation on computational results. Eliminating the additional error generation mechanisms due to turbulence modeling is beneficial in assessing the performance of a viscous flow solver.

Second order artificial dissipation terms for the solution of convection–diffusion equations in pressure based semi-implicit schemes are formulated to improve the numerical accuracy. It is clearly shown that reducing the artificial dissipation terms in a central differencing scheme will reduce the numerical dissipation error. In the present study, the lower limits of the artificial dissipation coefficient ε_2 were 0.1, 0.6, and 0.8 for the flows at Reynolds numbers of 790, 40,000, and 342,190.

Calculations accounting for the influence of streamline curvature are also presented. The primary modification in using the curvature correction model was found in the zones of secondary flow vortices.

The current turbulence model was not capable of capturing the flow field where a pair of passage vortices interacted with each other at 90° section at $Re = 342,190$. This may be caused by the an-isotropic turbulence property of three-dimensional and highly rotational complex flow field in this region. In general, the calculated results were in good agreement with the experimental data in regions other than the strong an-isotropy areas.

Curvature correction in turbulent flow may result in slight modifications in streamwise velocity distributions. Although the curvature correction near the concave surface has a tendency to modify the effective viscosity magnitude, it does not influence the area coverage of the turbulent flow in a significant manner in the duct.

Curvature correction on effective viscosity is significant in regions where the passage vortex is dominant. The core of the passage vortex and the peak in the effective viscosity distribution along the radial direction coincide.

Curvature corrections in streamwise velocity are non-negligible in the core of the passage vortex, concave wall boundary layer, top/bottom endwall-boundary-layer and in the interaction area between the passage vortex and convex wall. A 4–6% under-prediction of the streamwise velocity in the core of the passage vortex is apparent.

Turbulence generation in the 90° cross section is mainly controlled by the passage vortices and boundary layers.

For intermediate Reynolds number, the average magnitude of effective viscosity is three to six times smaller in turbulent flow area when compared to high Re number case.

The qualitative character of measured total pressure losses was captured by the numerical computations. Extremely high strain rates in this highly rotational fluid flow region increase the viscous losses and reduce the predictability of viscous flow. The overall "mushroom shape" of the passage-vortex/convex-wall interaction area is apparent in both measurements and computations.

Turbulent kinetic energy distributions from numerical computations were confirmed by turbulence measurements at high Reynolds number from three-sensor hot-wire measurements. The passage vortex interaction area in which numerical computations are challenging coincided with the areas containing highly an-isotropic turbulent flow as measured by a three-sensor hot-wire.

Near the core of the passage vortices and in the interaction zone between the passage vortices, three-dimensional re-circulatory flows are so dominant, a two-equation model originally developed from a pure shear flow idea is not sufficient.

Turbulent viscous flow features of the 90° turning duct flow can be predicted in a very effective manner in most of the exit cross section. The cores of the passage vortices and vortex/wall interaction areas are challenging to predict because of the difficulty in modeling an-isotropic turbulence created in highly strained flow areas.

NOMENCLATURE

A	Van Driest's constant
A_E, A_N, A_T A_W, A_S, A_B	coefficients for convection diffusion equation
b	mass flux
C_1, C_2, C_μ	turbulence modeling constants
C_P	specific heat at constant pressure
D	duct width
E	log-law coefficient
g	geometric relation between coordinates
G	contravarient velocity
G_k	turbulent production term

k	turbulent kinetic energy, TKE
p	static pressure
Pr	Prandtl number
r^*	normalized radial coordinate, $r^* = (r-r_o)/(r_i-r_o)$
r_i, r_o	inner, outer radius
R_c	radius of streamline curvature
Re	Reynolds number, $Re = \rho U_b D/\mu$
S_U, S_P	linearization coefficients of source term
S_ϕ	source term
u	velocity fluctuation in streamwise direction
U	streamwise mean velocity
U_D	normalized streamwise velocity difference, $U_D = (U/U_b)_{w/o} - (U/U_b)_w$
U_x, U_y, U_z	mean velocities in x, y, z-directions
V	electric potential
X, Y, Z	streamwise, radial and spanwise directions
x, y, z	cartesian coordinates
y_p	distance away from the wall
Γ	isotropic diffusion coefficient
Ω	vorticity
ε	turbulent dissipation rate
ε_2	coefficient of second order artificial dissipation term
ϕ	general scalar dependent variable
κ	von Karman constant
μ	molecular viscosity
μ_t	eddy viscosity
ξ, η, ς	transformed curvilinear coordinates
ρ	density
$\sigma_k, \sigma_\varepsilon$	turbulent Pr numbers for diffusion of k and ε
τ_w	wall shear stress

Subscripts

b	bulk
in,cl	inlet centerline
nb	neighbor points of point p
o	total condition
P	central point of control volume
p	first grid point away from the wall
$w/o, w$	without, with curvature effect correction
w	wall
∞	free-stream

Superscripts

$'$	correction
$*$	estimate
$+$	non-dimensionalized wall quantity

Other

e, w, n, s, t, b — center points between p and E, W, N, S, T, B in Figure 2

REFERENCES

Basson, A. H. (1992) Ph.D. Thesis, The Pennsylvania State University.

Briley, W. R. and McDonald, H. (1984) Three-Dimensional Viscous Flow with Large Secondary Velocity, *Journal of Fluid Mechanics*, **144**, 47–77.

Govindan, T. R., Briley, W. R. and McDonald, H. (1991) General Three-Dimensional Viscous Primary/Secondary Flow Analysis, *AIAA Journal*, **29**, 361–370.

Humphrey, J. A. C., Taylor, A. M. K. P. and Whitelaw, J. H. (1977) Laminar Flow in a Square Duct of Strong Curvature, *Journal of Fluid Mechanics*, **83**, 509–528.

Humphrey, J. A. C., Whitelaw, J. H. and Yee, G. (1981) Turbulent Flow in a Square Duct with Strong Curvature, *Journal of Fluid Mechanics*, **103**, 443–463.

Launder, B. E. and Spalding, D. B. (1974) The Numerical Computation of Turbulent Flows, *Comp. Meth. Appl. Mech. Eng.*, **3**, 269–289.

Leschziner, M. A. and Rodi, W. (1981) Calculation of Annular and Twin Parallel Jets Using Various Discretization Schemes and Turbulence-Model Variations, *ASME Journal of Fluids Engineering*, **103**, 352–360.

Mayle, R. E., Blair, M. F. and Kopper, F. C. (1979) Turbulent Boundary Layer Heat Transfer on Curves Surfaces, *The Transactions of the ASME Journal of Heat Transfer*, **101**(3), 521–523.

Patankar, S. V. and Spalding, D. B. (1972) A Calculation Procedure for Heat, Mass and Momentum Transfer in Three-Dimensional Parabolic Flows, *Int. J. Heat and Mass Transfer*, **15**, 1787–1806.

Patankar, S. V. (1980) *Numerical Heat Transfer and Fluid Flow*, Hemisphere Publishing Corp., New York.

Pouagare, M. and Lakshminarayana, B. (1986) A Space-Marching Method for Viscous Incompressible Internal Flows, *Journal of Computational Physics*, **64**(2), 289–415.

Pratap, V. S. and Spalding, D. B. (1975) Numerical Computations of the Flow in Curved Ducts, *The Aeronautical Quarterly*, **26**, 219–228.

Rhie, C. M. and Chow, W. L. (1983) Numerical Study of the Turbulent Flow Pass an Airfoil with Trailing Edge Separation, *AIAA Journal*, **21**, 1525–1531.

Taylor, A. M. K. P., Whitelaw, J. H. and Yianneskis, J. (1981) Measurement of Laminar and Turbulent Flow in a Curved Duct with Thin Inlet Boundary Layers, *NASA CR-3367*.

Thomann, H. (1968) Effect of Streamwise Wall Curvature Heat Transfer in a Turbulent Boundary Layer, *Journal of Fluid Mechanics*, **33**, Pt. 2, 283–292.

Van Doormaal, J. P. and Raithby, G. D. (1984) Enhancements of the SIMPLE Method for Predicting Incompressible Fluid Flows, *Numerical Heat Transfer*, **7**, 147–163.

Wiedner, B. G. (1994) Passage Flow Structure and its Influence on Endwall Heat Transfer in a 90° Turning Duct, Ph.D. Thesis, The Pennsylvania State University.

Wiedner, B. G. and Camci, C. (1996) Determination of Convective Heat Flux on Heat Transfer Surfaces with Arbitrarily Defined Boundaries, *ASME Journal of Heat Transfer*, **118**(4), 1–8.

Wiedner, B. G. and Camci, C. (1996) Passage Flow Structure and its Influence on Endwall Heat Transfer in a 90° Turning Duct: Turbulent Stresses and Turbulent Kinetic Energy Production, *ASME paper 96-GT-251*, International Gas Turbine Congress, Birmingham, UK.

Wiedner, B. G. and Camci, C. (1997) Passage Flow Structure and its Influence on Endwall Heat Transfer in a 90° Turning Duct: Mean Flow and High Resolution Endwall Heat Transfer Experiments, *ASME Journal of Turbomachinery*, **119**(1), 39–50.